WPMST1-CPR(18) 19295

M Komm et al.

Divertor impurity seeding experiments at the COMPASS tokamak

Preprint of Paper to be submitted for publication in Proceeding of
27th IAEA Fusion Energy Conference

This work has been carried out within the framework of the EUROfusion Consortium and has received funding from the Euratom research and training programme 2014-2018 under grant agreement No 633053. The views and opinions expressed herein do not necessarily reflect those of the European Commission.

Divertor impurity seeding experiments at the COMPASS tokamak

M. Komm[1], I. Khodunov[1,2], J. Cavalier[1], P. Vondracek[1,3], S. Henderson[4], J. Seidl[1], J. Horacek[1], D. Naydenkova[1], J. Adamek[1], P. Bilkova[1], P. Bohm[1], A. Devitre[2], M. Dimitrova[1,5], S. Elmore[4], M. Faitsch[6], P. Hacek[1,3], J. Havlicek[1], A. Havranek[1], M. Imrisek[1,3], J. Krbec[1,7], M. Peterka[1,3], R. Panek[1], T. Popov[5,8], O. Samoylov[2], M. Sos[1,7], M. Tomes[1,3], K. Tomova[2], V. Weinzettl[1] and the EUROfusion MST1 team[9]

[1] Institute of Plasma Physics of the CAS, Za Slovankou 3, 182 00 Prague 8, Czech Republic
[2] Department of Applied Physics, Gent University, Gent, Belgium
[3] Charles Univ, Fac Math & Phys, V Holesovickach 2, 180 00 Prague 8, Czech Republic
[4] Culham Sci Ctr, CCFE, Abingdon OX14 3DB, Oxon, England
[5] Emil Djakov Institute of Electronics, Bulgarian Academy of Sciences, 72, Tsarigradsko Chaussee, 1784 Sofia, Bulgaria
[6] Max-Planck-Institut fur Plasmaphysik, 85748 Garching b. Munchen, Germany
[7] FNSPE, Czech Technical University in Prague, Brehova 7, Czech Republic
[8] Sofia Univ St Kliment Ohridski, Fac Phys, 5 J Bourchier Blvd, Sofia 1164, Bulgaria
[9] See the author list of Meyer H. et al 2017 Nucl. Fusion 57 102014

E-mail: komm@ipp.cas.cz

Abstract. Partial detachment is the desired regime for the baseline burning plasma scenario in ITER and next-step devices, as it allows to disspate the majority of the energy carried by charged particles through the scrape-off-layer (SOL) and thus avoids localised heat flux deposition in the divertor region. The COMPASS tokamak is equipped with an open divertor and has a relatively short connection length, both factors being unfavourable for access to detachment. As such, it only allows to approach naturally detached operation at very high line-averaged densities ($> 10^{20}$ m^{-3}), which are incompatible e.g. with maintaining the ELMy H-mode regime. In order to achieve the detachment at lower densities, impurities (such as nitrogen) should be injected into the plasma in the divertor region.

A series of experiments with impurity injection in the range of 1-9$\times 10^{20}$ molecules per second at different locations in the divertor were performed with the aim to cool the plasma and influence the particle and heat transport onto the divertor targets and provoke partial detachment. Previously reported results [M. Komm et al, EPS 2017, P1.118] were largely extended by injection of nitrogen at the outer divertor target.

In order to analyze the divertor heat flux footprint in seeded plasmas, we introduce a buffered heat flux q_B, which is approximated by an exponential decay.A new set of generic parameters - the peak heat flux q_{peak}, the fraction of power reaching the target f_{div} and divertor footprint spreading factor S_f was proposed to characterise divertor footprint under detached conditions.

Submitted to: *Nuclear Fusion*

1. Introduction

The power exhaust in the divertor represents one of the key challenges of contemporary fusion research, as the heat fluxes in large machines, such as ITER or DEMO, can easily exceed the material limits of the plasma-facing components (PFCs) and lead to their damage and reduced lifetime [13]. Most of the heat flux escaping from the last closed flux surface (LCFS) is carried along the field lines until it reaches the PFCs in the divertor. To overcome this issue of divertor overheating in ITER, the partially detached regime is envisaged in the baseline scenario for burning plasmas [14]. Detachment allows to convert a majority of the energy carried by charged particles into radiation and as such prevents localised deposition of the heat fluxes [15]. It is characterised by an electron temperature gradient along the field lines, as they pass from the scrape-off layer (upstream) to the divertor target (downstream) and significant power loss in the SOL. The temperature at the target is typically low (< 5 eV), allowing a significant population of neutrals to form in the divertor region.

In general, there are two ways of achieving the detached regime - (i) by increasing the density until sufficient amount of collisions with charged and neutral particles leads to power dissipation and cooling of the downstream plasma, or (ii) by injection of selected impurities, often strong radiators, which also allows to remove the power by radiation. In this work, we will focus on the latter approach, and we will present results of impurity seeding experiments at the COMPASS tokamak, where access to detached operation is particularly difficult due to open divertor geometry and relatively short connection length. On the other hand, COMPASS has a ITER-like plasma shape and as such it can contribute to improve or formulate the relevant multi-machine scalings.

The physics of detachment is incredibly complex, including atomic physics, surface geometries and plasma-wall interaction. The aim of this contribution is to characterise the practical aspects of detachment, such as the reduction of plasma pressure and heat fluxes in the divertor. In order to do this, we introduce a novel set of generic parameters: peak divertor heat flux q_{peak}, total power reaching the divertor P_{div} and distance characterising the width of power deposition ΔS, which are able to describe important properties of virtually any profile, independently of the underlying physics processes.

2. Experimental setup

2.1. Injection scenario

The impurity was injected in a series of otherwise identical attached L-mode discharges (I_p=-210 kA, B_T=-1.38 T, n_e=5$\times$10^{19} m^{-3}). After a series of comparative experiments with nitrogen and neon seeding, the nitrogen was selected as a more favourable impurity (allowing for a range of effects in the divertor without the risk of disruptions) and all the experiments in this work refer to discharges with nitrogen seeding. The impurity particle flux was controlled by a pre-set waveform on a piezoelectric valve in the range of 1-9$\times$10^{20} molecules per second. A typical waveform included a 10 ms pre-puff during which the valve was requested to be fully opened (to ensure that the valve mechanism starts to function properly), followed by a

100 ms constant puff at the desired particle flux, which was varied on a shot-to-shot basis. Two different seeding locations were used: at first nitrogen injection at the inner target (major radius R=469 mm) [1], later at the outer target (R=500 mm), located outside the outer strike point. For reference in the future sections, we include the list of performed discharges in the summary table 1.

Table 1. List of discharges performed with LFS anf HFS nitrogen seeding

HFS seeding		LFS seeding	
Discharge	Γ_{N_2}	Dischagre	Γ_{N_2}
—		#15972	1.4×10^{20} s^{-1}
#13729	2.0×10^{20} s^{-1}	#15973	2.0×10^{20} s^{-1}
#13725	2.8×10^{20} s^{-1}	#15975	2.6×10^{20} s^{-1}
#13730	3.7×10^{20} s^{-1}	#15976	3.2×10^{20} s^{-1}
#13731	4.5×10^{20} s^{-1}	#15977	4.4×10^{20} s^{-1}

2.2. Influence of nitrogen content on probe measurements

The divertor probes are the principal diagnostics for this type of studies. COMPASS is equipped with two different probe arrays: (i) the array of 39 Langmuir probes, which are operated in swept mode and analysed using the first derivative probe technique (FDPT) [2] and (ii) a combined array of 55 Ball-pen and 110 Langmuir probes (LP) (in two linear arrays), where the measurement of electron temperature is based on difference between the floating potential of the Langmuir and Ball-pen probes (BPP) [3].

The analysis of probe measurements in tokamaks is usually based on an assumption of plasma consisting of single ion species. This can be clearly violated in case there's intensive injection of nitrogen in deuterium plasmas. Unfortunately, it was not possible to determine the fraction of nitrogen ions at the location of probe measurements. However, we can model the effect of variable fraction of nitrogen in plasma and hence estimate the error which can be made by neglecting the presence of nitrogen in the analysis. In order to do that, we assume that the nitrogen is only singly ionized (which corresponds to the most probable state of nitrogen in the range of temperatures measured during the seeding phase) and we introduce the nitrogen density fraction $f_N = n_N/n_i$. We further assume that the only effect of nitrogen is a presence of ion current carried by nitrogen ions to the probes, omitting possible effects on ion collecting area, collisional effects in the sheath etc.

In case of temperature measurements achieved using a combination of floating potentials of the Ball-pen and a Langmuir probes (LP), with the knowledge of a coefficient α_{LP}[3]. The value of the LP floating potential is influenced by the presence of nitrogen ions and scales as

$$V_{fl} \sim ln\Big((1-f_N)\sqrt{m_D/m_e} + f\sqrt{m_N/m_e}\Big)/ln(\sqrt{m_D/m_e}), \quad (1)$$

where m_D and m_N are deuterium and nitrogen mass respectively. In absence of working theoretical model for the Ball-pen probe, we assume that coefficient α_{BPP} scales equally.

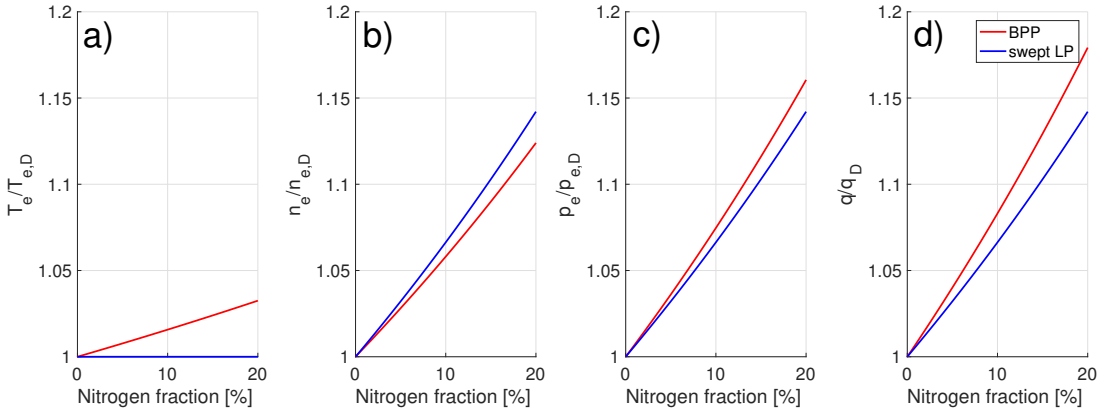

Figure 1. Imprecission of measurement of T_e (A), n_e (B) and p_e (C) for swept Langmuir and Ball-pen probes due to presence of nitrogen in the plasma. All values are normalized to measurements in pure deuterium.

This means that the total coefficient $\alpha = \alpha_{LP} - \alpha_{BPP}$ increases with increasing amount of nitrogen in the plasma. Since the dependence is logarithmic, only small variations of V_{fl} occur within the range of expected nitrogen fractions ($f_N < 20\%$) as shown in Fig. 1A. The measurement of electron temperature from swept Langmuir probe is not affected, as it operates with a ratio $I(V)/I_{sat}$, where I_{sat} is also determined experimentally and so it reflects the plasma conditions correctly.

A similar effect occurs when density is extracted from the measurements of ion saturation current. In this case the effective mass influences the ion sound speed and so the density scales as $\sim 1/\left(1-f+f\sqrt{m_D/m_N}\right)$ (shown in Fig. 1B). This effect is present for both probe techniques, however in case of LP+BPP, the effect is partially mitigated by a small influence of T_e measurement described in previous paragraph.

Finally, when these two influences are combined, the resulting error in electron pressure and heat flux measurement is shown in Figs. 1C and 1D respectively. It can be observed that both techniques have different deviations from the optimal measurement, however the scale of introduced error is acceptable even for relatively large ($\sim 20\%$) concentrations of nitrogen.

2.3. Comparison of divertor probe diagnostics

Given the different modes of operation, it is useful to cross-check whether the two diagnostics (swept probes and combined LP+BPP probes) are delivering the same results when employed at the same time in the same radial location at the outer target. For this purpose, a set of measurements in the vicinity of the outer strike point (OSP) (within 2 cm outside the OSP) was selected. The data were selected from the shots where nitrogen seeding was employed, both from the HFS and LFS seeding scans. The results from LP+BPP arrays were averaged over the time of sweeping of the swept LPs. When the FDPT detected a bi-Maxwellian distribution of electrons, only the higher temperature component was considered. The results

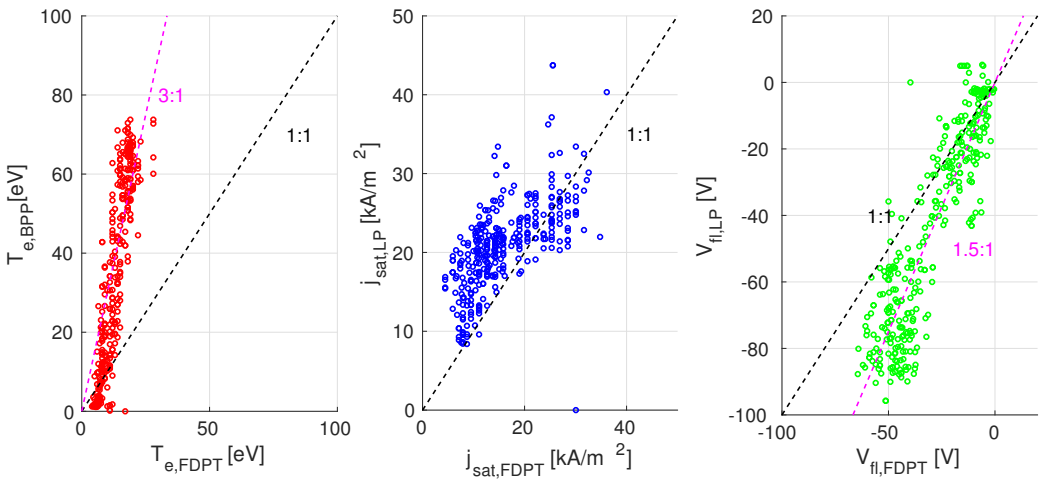

Figure 2. Comparison of measurements of electron temperature (a) and j_{sat} (b) and V_{float} (c) by the two different arrays of divertor probes.

for T_e, j_{sat} and V_{float} are presented in Fig. 2. It can be seen that while all quantities are reasonably well correlated between the two diagnostics, in case of T_e, the BPP+LP array gives approximately $3\times$ higher temperature than the swept LPs. Also, the floating potential exhibits a systematic difference at low values (these correspond to peak temperatures at the OSP), which indicates that there is indeed a fundamental difference between measurements of the two probe arrays. Several hypotheses were drawn, pointing to the role of different LP geometry or possible existence of intrinsic toroidal asymmetry in COMPASS, however the exact root of this discrepancy is not well understood at the time of writing. We will further assume that the discrepancy could be remedied by some constant factors employed in future analysis and concentrate the discussion on relative changes of both pressure and heat flux in the divertor, rather than on analysis of its absolute values.

2.4. Upstream measurements

With respect to the upstream measurements, the major source of error is the determination of the location of the LCFS. Since the low-density plasmas in COMPASS are in the sheath-limited regime, it is not possible to determine the separatrix temperature from power balance as in larger machines [11]. Instead, the location of LCFS is determined from equilibrium reconstruction code EFIT, which is known to have limited precision. We will assume that the possible imprecision of the separatrix location is of systematic nature (at least in the range of studied discharges)[17] and we will focus on relative changes of upstream quantities.

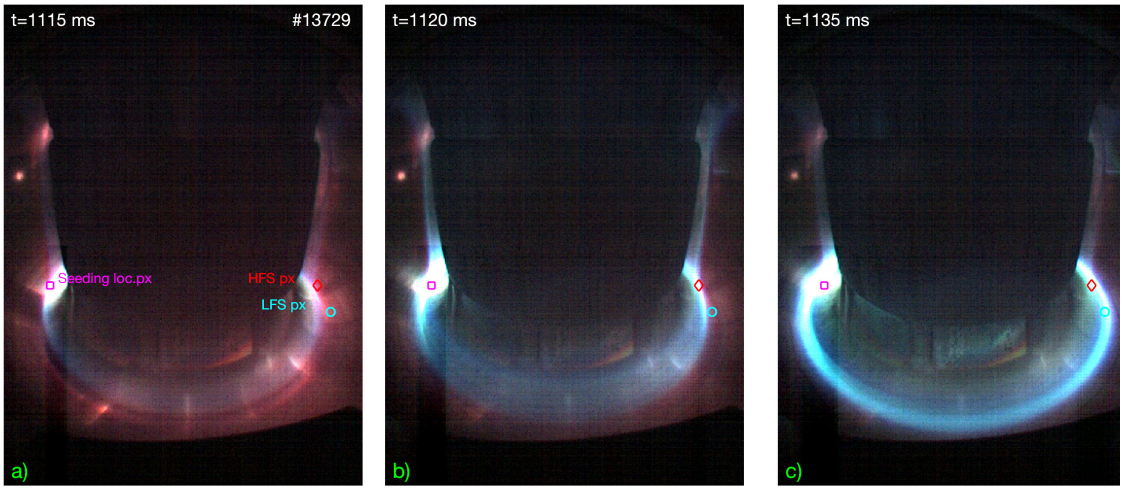

Figure 3. Three different patterns of nitrogen radiation in discharge #13729 (Γ_{N_2} = 2.0 × 10^{20} m^{-3}) observed by RIS1 camera with marked locations of seeding, LFS and HFS pixels.

3. Effects of the seeding

3.1. Radiation measured by the visible cameras

The location of nitrogen injection is in the field of view of the RIS system[5] - a pair of fast color cameras operating in the visible range. One camera was oriented with tangential field of view of the plasma, while the other was providing wide angle radial view. The RIS1 camera operated at 8 kHz sampling frequency with resolution 1280×624 RGB pixels, which RIS2 was set to 5 kHz with resolution of 1280×1000 pixels. It was possible to identify 3 different patterns of radiation during nitrogen injection, which are shown in Figs. 3 and 4. The piezoelectric valve was requested to open at t=1100 ms and after approximately 15 ms it was possible to detect a new source of radiation around the injection location (Fig. 3A). Later, this radiation became more toroidally uniform but was restricted to the HFS (Fig. 3B), even in the cases when the injection was located at the outer strike point. In addition, measurements by the second RIS camera (see Fig. 4) shows that the radiation is not limited to the inner target but extends up to the whole HFS SOL. In some discharges, where the amount of injected nitrogen was sufficient, there was an abrupt change of the radiation pattern and the radiation became centred around the x-point region (Fig. 3C). This transition was accompanied by a sudden change of temperature measured by the divertor probes, as shown in Fig. 5, for the discharge #13729 (HFS seeding $\Gamma_{N_2} = 2.0 \times 10^{20}$ s^{-1}), where several such transitions were observed, since the amount of injected nitrogen was probably marginal with respect to detachment access. The pixel signal intensities (the total intensity from RGB channels was used) indeed follow this behaviour (patterns are labeled HFS and LFS in the figure) and at some times exhibit low-frequency oscillations (f ∼1 kHz), which according to RIS data are axisymmetric and ressemble those measured at AUG[31]. For the definition of T_e plotted in Fig. 5 see section 3.4.

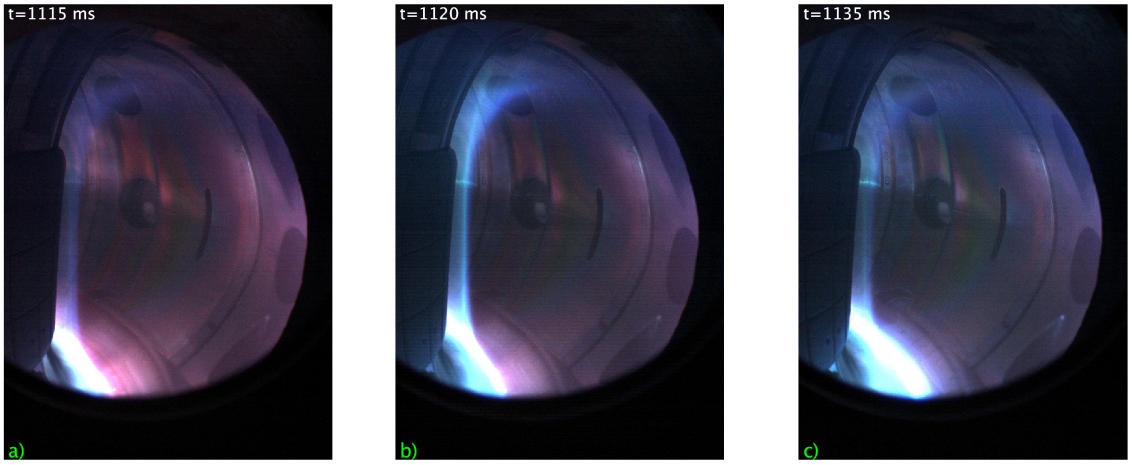

Figure 4. Three different patterns of nitrogen radiation in discharge #13729 observed by the RIS2 camera.

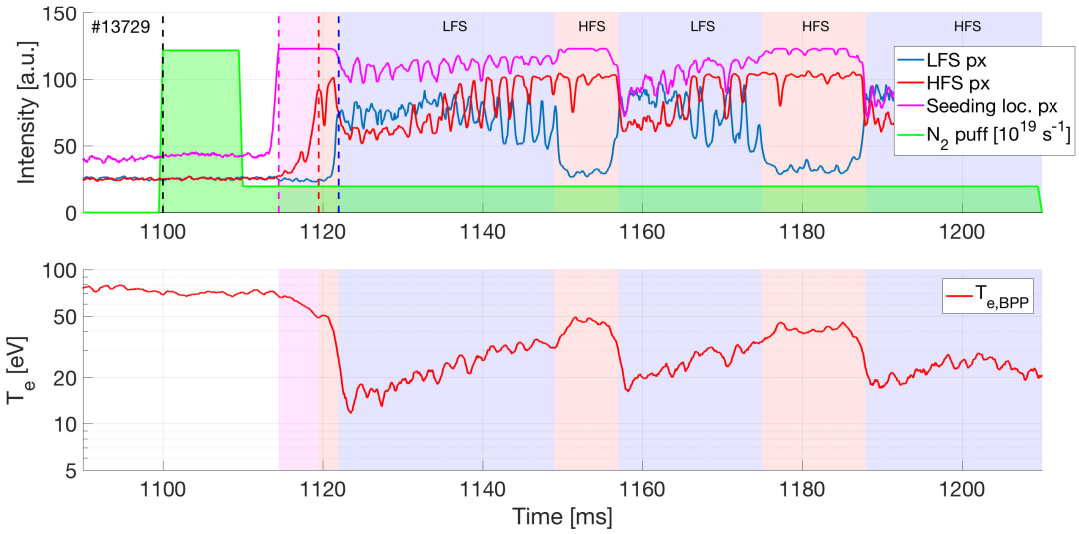

Figure 5. Pixel intensity at seeding location, HFS and LFS (top) and evolution of T_e at LFS target (bottom). Background colors and labels indicate radiation regimes shown in Figs.3 and 4.

3.2. Spectroscopy measurements

The radiation of nitrogen was measured using a set of mini-spectrometers for near UV (247-473 nm), visible (460-663 nm), and infra-red (630-680 nm) ranges with resolution of 0.15, 0.17, and 0.23 nm, respectively [25]. The field of view covers the edge plasma at the outer midplane but excludes the outer target, as shown in 6B. It was possible to identify several nitrogen lines in the measured spectrum (see 6A). The most intensive line measured in the near UV to blue visible spectrum was the N IV multiplet lines near 348 nm, with much weaker contributions from the N III multiplet lines near 410 nm and the N II singlet line at

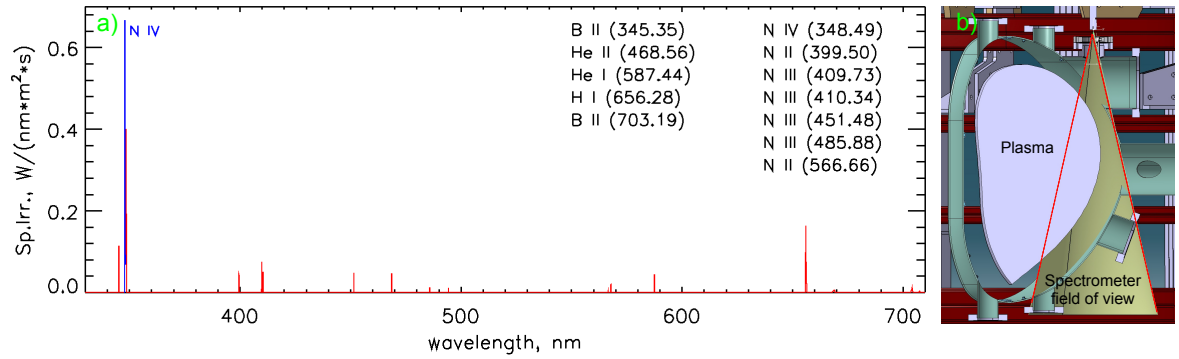

Figure 6. Nitrogen lines identified in the measured spectrum in discharge #15976 at t=1150 ms (a) and the field of view of the minispectrometers (b).

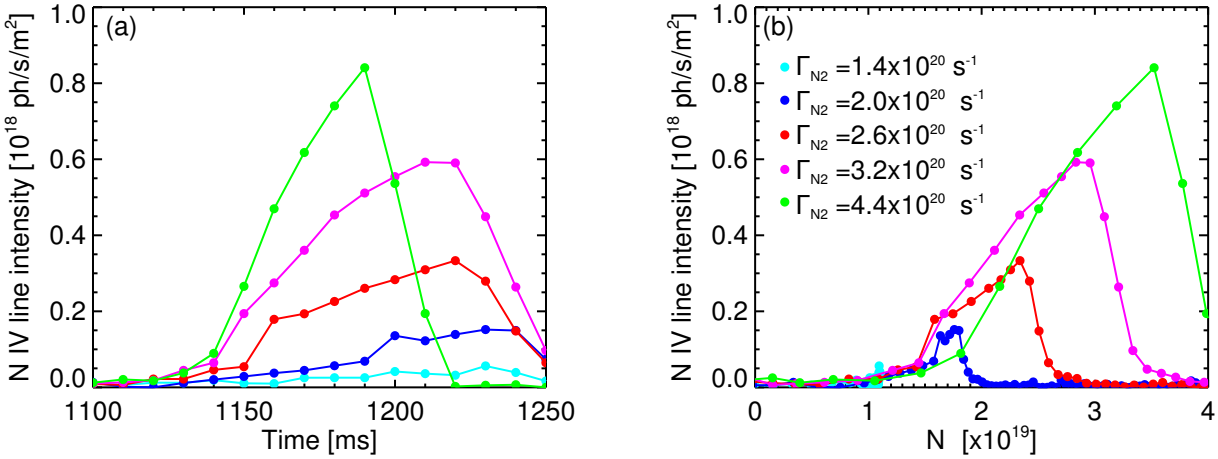

Figure 7. The intensity of the N IV multiplet line at 348 nm evolving in time (a) and as a function of nitrogen content (b).

399.5 nm. The qualitative behaviour of the N IV multiplet intensity follows the amount the injected N_2 for each shot, as shown in Fig. 7A and Fig. 7B.

We use the line-of-sight measuring the separatrix and select the time slice near the beginning of the N_2 seeding window (t=1150 ms) in shot #15976 to discuss the model and necessary assumptions for estimating the N concentration based on the N IV multiplet intensity. The N concentration, c_N, can be calculated using:

$$c_N = \frac{I_{NIV}}{f_{N3+}PEC^{exc} + f_{N4+}PEC^{rec}} \frac{1}{\Delta L n_e^2} \tag{2}$$

where I_{NIV} is the N IV multiplet intensity, $f_{N3+,4+}$ are the ion fractional abundances of the Z=3+,4+ N ions, $PEC^{exc,rec}$ are the photon emissivity rate coefficients for excitation and recombination, and ΔL is the length of the N IV emitting region through the line-of-sight.

Firstly, to calculate the N IV multiplet intensity, a 4-Gaussian fit of the N IV multiplet emission feature and a single Gaussian fit of the nearby B II line is carried out as shown in Fig. 8A. Next, the ADAS excitation and recombination rates for this transition are interpolated as a function of temperature in Fig. 8B. From HRTS measurements at this particular time slice and

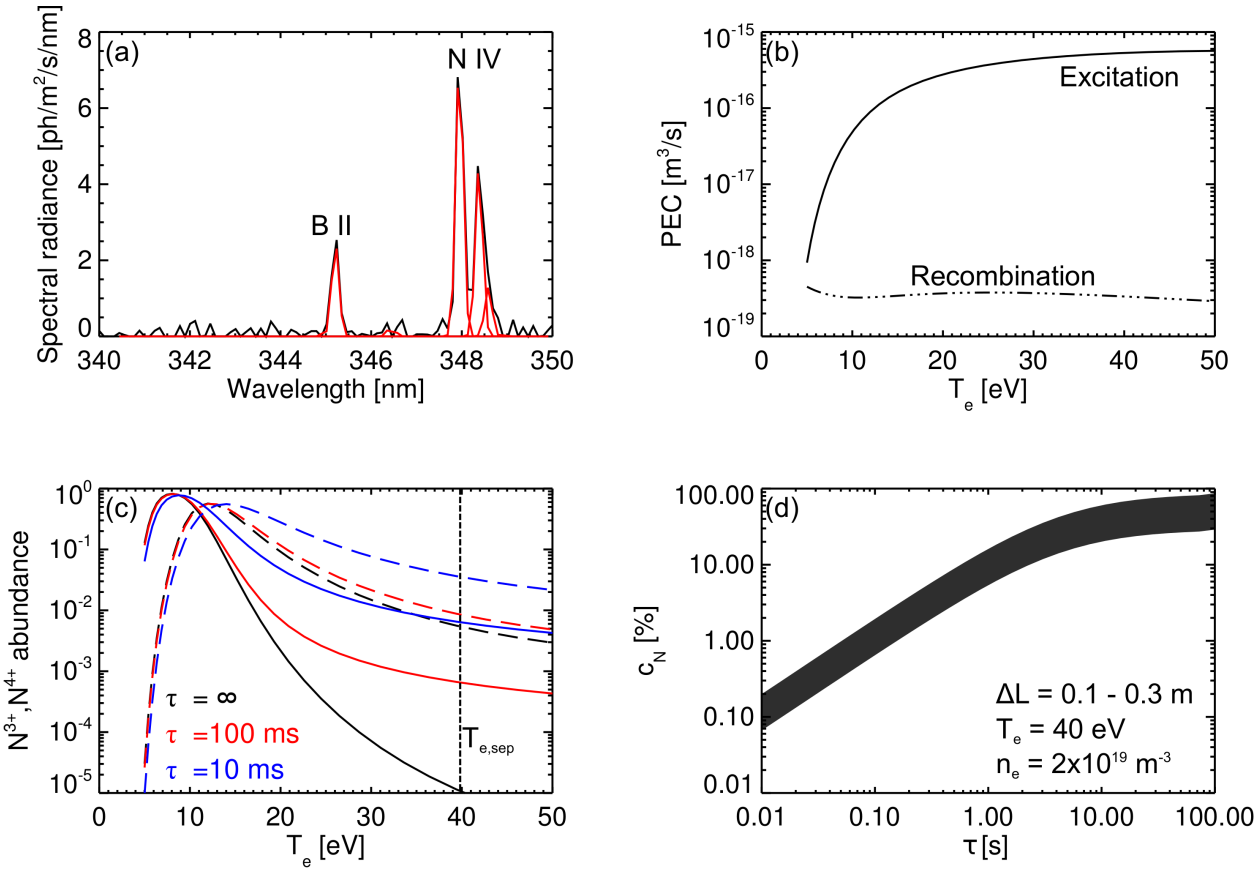

Figure 8. The measured spectral radiance (black) with Gaussian fit components (red) measured in the near UV for shot #15976 at t=1150 ms is shown in (a). Excitation and recombination rates for the N IV multiplet transition at λ ~348 nm are shown as a function of Te for n_e=2×10^{19} m^{-3} in (b). The ion fractions of N^{3+} (solid) and N^{4+} (dashed) are shown in (c) for three different impurity residence times. The N concentration at T_e=40 eV is shown as a function of τ in (d).

shot, the separatrix density is $n_{e,sep}$ ~2×10^{19} m^{-3}, while the temperature is $T_{e,sep}$ ~40 eV. The fractional abundance of the $N^{3+,4+}$ charge states are then calculated using an ionisation balance with a transport loss term, $n_e\tau$, where τ is the impurity residence time in the separatrix. This parameter is not well known in the separatrix, or indeed anywhere in the SOL; however, one could begin by estimating it using the typical particle confinement times which range from 5 - 15 ms in COMPASS. In theory, this parameter could also account for enhanced recombination due to neutral deuterium atoms in the separatrix. For this study, the ion fractions for three τ values of 10, 100, ∞ ms are shown in Fig. 8C by the red, blue, and black lines, where the solid and dashed lines represent the N^{3+} and N^{4+} charge states, respectively. The latter τ value represents the zero-transport case where only ionisation and recombination rate coefficients from ADAS are considered.

The c_N calculated at $T_{e,sep}$=40 eV is shown in Fig. 8D as a function of τ. The shaded region shows the upper and lower limit of ΔL=0.1 - 0.3 m. The c_N is unphysically high (close to 100%) in the zero-transport case (τ >10 s) suggesting that transport must be included.

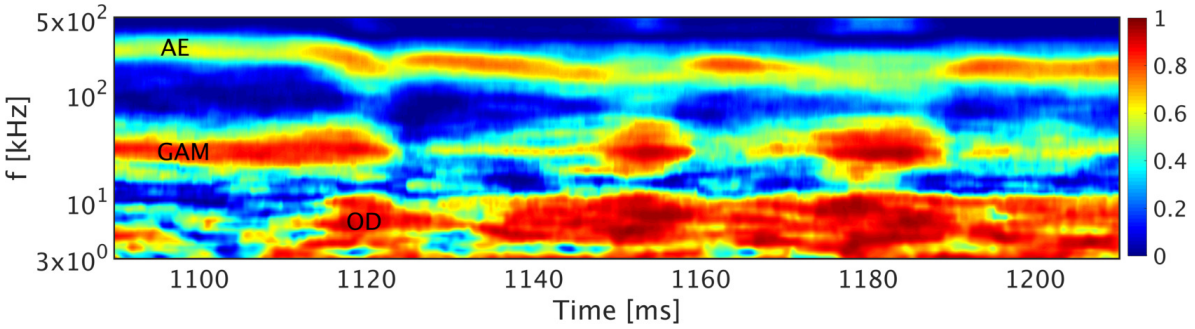

Figure 9. Wavelet cross-coherence between two Mirnov coils (MC17 and MA17), toroidally separated by 135° and located in the HFS divertor region of COMPASS (#13729).

Between τ=10 - 100 ms, the c_N varies from 0.1 - 1.0% in the separatrix, which is likely a lower limit on the divertor nitrogen concentration since the ratio of the nitrogen concentration in the divertor and core plasma volumes has been observed on AUG to reach values of 10 [33]. These first results therefore provide a first insight into the divertor N concentrations required for detachment on COMPASS, however additional spectrometer sightlines isolating the emission from the divertor volume (e.g. following the analysis of [34]) and core CX measurements of the nitrogen density would help to validate these estimations.

3.3. Magnetic measurements

COMPASS is equipped with 2 sets of non-integrated Mirnov coils toroidally separated by 135°, each composed of 24 coils located in the same poloidal cross section (see Fig. 1 in [36]) that allow studies of the poloidal magnetic field generated by instabilities that take place during the discharge duration. In Fig. 9, we present the wavelet cross-coherence between the two toroidally separated Mirnov coils 17, located in the HFS divertor region of COMPASS, that shows how different instabilities during a nitrogen seeding experiment. One can observe that the MHD activity is strongly influenced by the nitrogen injection. Related to the first temperature drop ($\sim$1120 ms), a strong mode develops around 6 kHz (labeled OD as onset of detachment) and grows back every time the transition between attached and detached plasma occurs ($\sim$1155 and 1187 ms). The geodesic acoustic mode [36] (labeled GAM around 30 kHz) also strengthens during every onset of detachment while the Alfen eigenmode [37][38] (labeled AE around 250 kHz) is damped. Between each divertor temperature drops, the GAM almost fully disappears while the AE mode builds up but with a lower frequency than prior to nitrogen seeding.

In nitrogen seeding experiments during H-mode [39] and also in density ramp-up L-mode [40] on ASDEX Upgrade, strong fluctuations around 6 kHz were observed by AXUV detectors near the x-point during the transition from attached to completely detached plasma. This phase called by the ASDEX team the *fluctuating detachment state* [42] seems to be linked to the development of the current convective instability [43]. As described in [43][44][45], such an instability develops when a large temperature difference exists between the inner and outer divertor, i.e. when the inner divertor detaches, as it usually detaches prior the outer one.

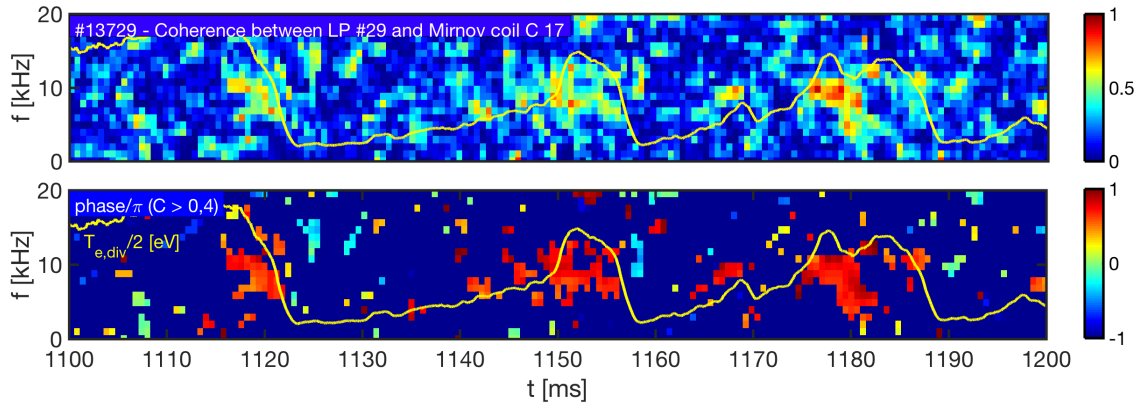

Figure 10. Coherence measurements: cross-coherence between T_e measurement near the LFS strikepoint of #13729 and the Mirnov coil MC17 (A) and associated phase divided by π (B). Yellow line indicates T_e measured by div. probes (divided by factor 2).

Once the outer divertor detaches too, the temperature difference vanishes and the instability stabilises, so that the fluctuations disappear.

The mode visible around 6 kHz in Fig. 10 seems to have a similar behaviour as the fluctuating detachment state described above since it appears mainly during the temperature drop in the divertor region. In addition, AXUV detectors looking near the X-point region also detect these fluctuations indicating that they take place at this location. Studies of the toroidal mode number with Mirnov coils show that the mode is toroidally symmetric. Last, the signals coming from the different poloidally separated Mirnov coils seem to indicate that the instability is mostly present in the divertor region (coils 16-21) but also in the top part of the vessel (coils 5-10).

In Fig. 10, we show the coherence between the Mirnov coil MC17 and T_e in the outer divertor measured by the combination of Ball-pen and Langmuir probes at R=483 mm. The mode is strongly visible at the onset of detachment when the mean T_e significantly drops. The fluctuations are also visible in the HFS divertor since the coherence between MC17 and a floating potential measurement near the HFS strike point shows a similar picture as shown in Fig. 9. The density, however, does not show any such fluctuations in both HFS and LFS indicating that the process is mainly linked to the temperature, supporting the physical picture described by [43].

3.4. Effects in the divertor

Figure 11 summarises the effects of nitrogen seeding on divertor temperature, pressure and heat flux, as measured by the combination of Langmuir and Ball-pen divertor probes. The values plotted in the figures correspond to the maximum quantities within 2 cm outside the OSP. The electron pressure was calculated as

$$p_e = (1 + M^2) n_e T_e, \tag{3}$$

where M is the parallel Mach number, which was assumed to be equal to 1 at the target

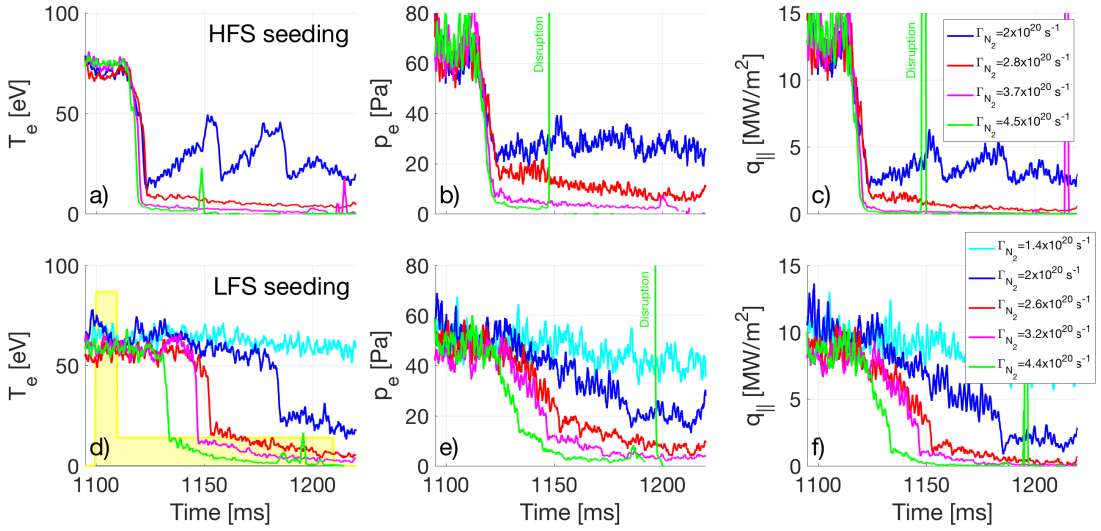

Figure 11. Temporal evolution of T_e, p_e and $q_{||}$ in the divertor for seeding at HFS (a-c) and LFS (d-f) measured by probes in the vicinity of the outer strike point.

due to Bohm condition and equal to 0 upstream. The heat flux was calculated from the measured values of T_e and j_{sat}. For simplicity it was assumed that the tiles were in ambipolar condition and so the parallel heat flux can be calculated as

$$q_{||} = \gamma j_{sat} T_e \tag{4}$$

The value of sheath heat transmission coefficient γ depends on the ratio T_i/T_e and the coefficient of secondary emission [8]. We assume that the secondary emission is negligible due to the small angle of incidence of the field lines with respect to the tile top surface (1-3°) [9] and that due to its high collisionality the plasma is isothermal, similarly to the conditions in MAST [10]. This yields value of γ equal to 7. This approach neglects a number of details (such as the role of local non-ambipolarity), which may become important under certain conditions, however in our analysis we will concentrate on such properties of the heat flux profiles, which are not affected by a possibly different value of γ, as long as it is constant along the target.

The effects of the impurities are dependent on the location of the seeding. When the impurity was introduced at the HFS, it was always followed by an abrupt change of temperature (Fig. 11A) at the outer target, similar to behaviour which was observed at DIII-D[19]. For the highest amount of seeding, the discharge was ended prematurely due to a disruption caused by mode locking of a tearing mode.

When the nitrogen was seeded at the LFS, the effects in the divertor were generally more gradual (Fig. 11D-F). The abrupt response on the T_e is still present but the relative magnitude of the drop is smaller and occurs at different times depending on the amount of nitrogen influx. At low seeding values there are no relaxations observed (unlike the case of HFS seeding, as shown in Fig. 11A-C), instead the target pressure and heat flux only gradually decrease. At

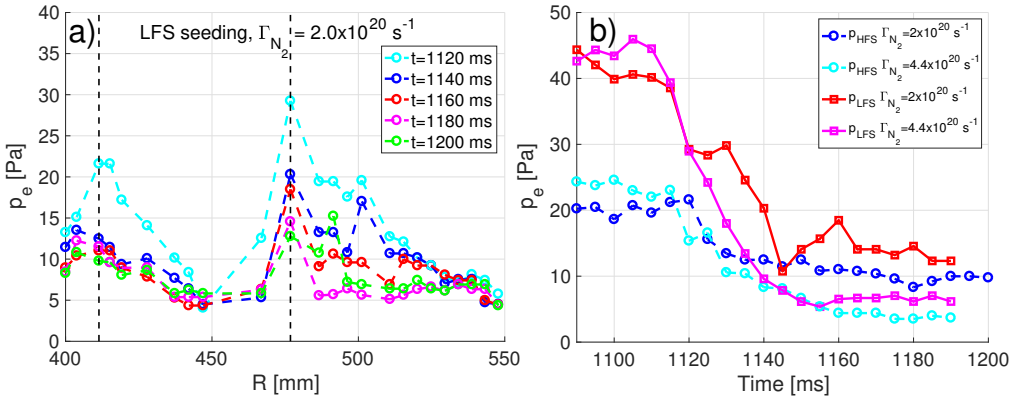

Figure 12. Profiles of electron pressure at different times (A) and the pressures measured at the inner and outer target (B) by the swept probes.

highest amount of seeding there is still a disruption but it occurs only at the end of the flat-top phase of the discharge.

Tokamaks with close divertor geometry, such as AUG[31] or JET[32] observe varied behaviour of the inner and outer target with respect to detachment access. Typically, the inner target detaches first (in density ramp-up scenarios) or at lower amount of seeded impurities. In order to investigate this effect at COMPASS, the array of swept divertor Langmuir probes was used. The probe array of combined Langmuir and Ball-pen probes does also cover the inner target, however the interpretation of these measurements remains unclear.

The profiles of pressure measured by the swept probes (as shown in Fig. 12A) show that the peak values of pressure on both targets are quite similar and they both exhibit a reduction during the course of nitrogen injection. Two probes were selected to follow the temporal evolution of the pressure: probe #5 at the inner target (R=415 mm) and probe #23 at the outer target (R=496 mm). The electron pressures measured by these probes are plotted in Fig. 12B for all the discharges in the LFS seeding scan. Within the data scatter it is difficult to identify strong trends but the pressure drop at the LFS is clearly larger than at the HFS and tends to be more gradual. The behavior at the HFS is more abrupt but not so pronounced as on AUG and JET. This is probably a consequence of an open divertor geometry, which prevents complete separation of the two targets.

3.5. Upstream and core parameters

Due to the proximity of the seeding location to X-point and relatively low edge plasma temperatures in Ohmic plasmas, it was expected that some of the injected nitrogen may penetrate into the confined plasma and cool it by radiation. As a consequence, a pressure drop would be observed on the upstream profile. This was confirmed by measurements performed by the horizontal reciprocating manipulator equipped with the probe head featuring a combination of Ball-pen and Langmuir probes[18]. The probe head was only allowed to probe far SOL to avoid possible perturbation of the divertor measurements. The position of LCFS according to the EFIT reconstruction was at R=0.728 m, however the true position is

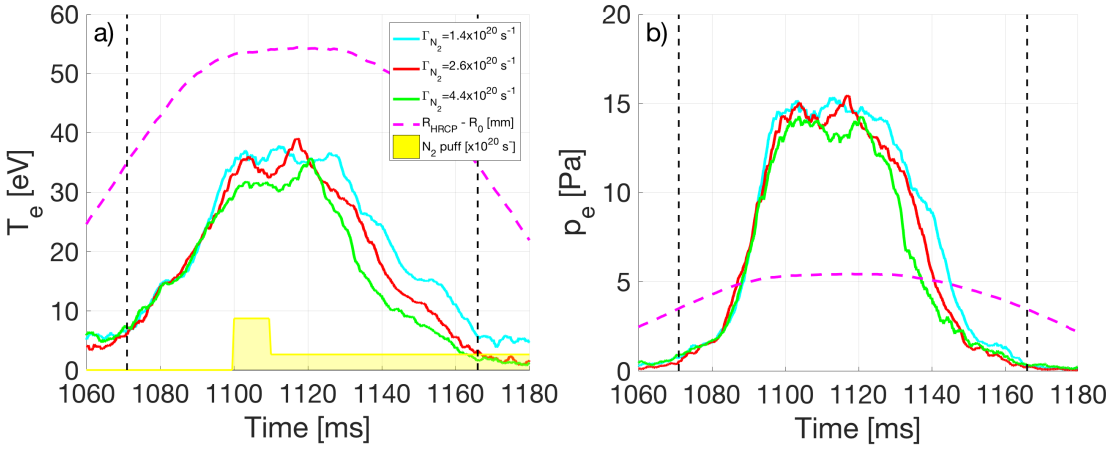

Figure 13. Time evolution of T_e and p_e during the movement of the HRCP. The vertical dashed lines indicate times where the probe penetrated beyond the limiter shadow.

expected to be ∼2 cm further outward[17]. Note that the radial position of the probe R_{hrcp} in Fig. 13 is plotted relative to the parking position R_0=800 mm. The probe was moving during the discharges with seeding at LFS in such timing, that the inward motion was performed before the beginning of seeding, while the outward movement occurred during the seeding. Unfortunately the effect of nitrogen upstream was gradual over the duration of the movement (see e.g. Fig. 11D-F), and so it was not possible to extract a true radial profile of the measured quantities during the outward motion. However, the time evolution of T_e and p_e as shown in Fig. 13 demonstrate a reduction of both quantities during the outward motion, depending on the amount of injected nitrogen. The electron pressure was calculated as in eq. 3. The density was deduced from the measurement of ion saturation current of a Langmuir pin assuming $T_i/T_e = 2$ and the effective collecting area given by a recently developed model[16].

Another indication of the radiation in the confined plasma is provided by measurements of power dissipated by radiation inside the LCFS $P_{rad,insep}$, which is calculated by tomographic reconstruction of the AXUV bolometers data[4] . Also, measurements of the Ohmic power P_{ohm}, obtained by magnetic measurement of U_{loop}, should show an increase due to higher Z_{eff} caused by the presence of nitrogen. Both effects are well visible in the profiles presented in Fig. 14. Note that in #15976 (magenta line in Fig. 14A), the initial radiation was significantly higher than in other discharges in the scan, however the relative change which occurred after the beginning of seeding is in line with trends observed in other discharges.

3.6. Upstream and downstream pressure

Findings presented during the previous section casted doubts whether the pronounced change in divertor parameters is due to nitrogen radiating in the SOL or whether the whole edge plasma is cooled. In order to distinguish between these two possibilities, the measurements of upstream and downstream pressures were compared.While the change of peak electron pressure at the outer target was monitored using the LP+BPP divertor probes, the upstream

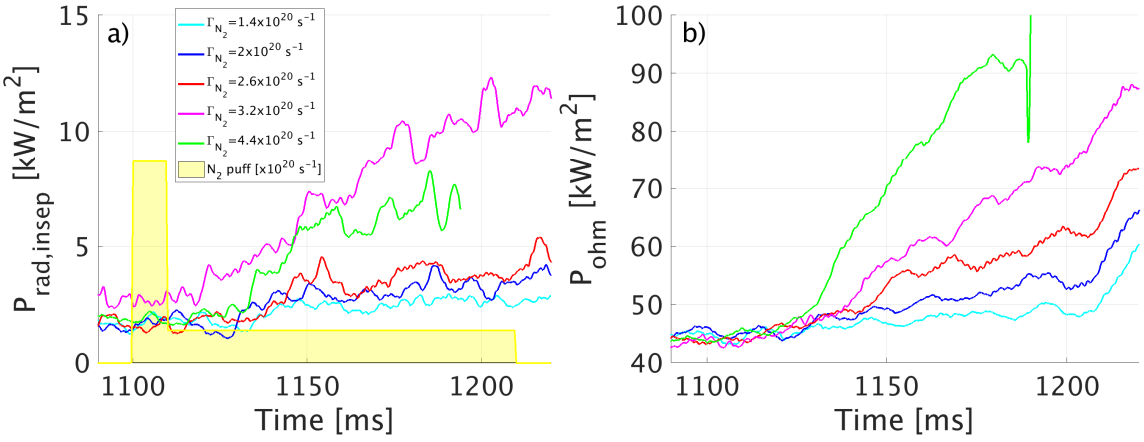

Figure 14. Time evolution of the plasma radiation measured by AXUV bolometers (left) and measurements of Ohmic power P_{rad}.

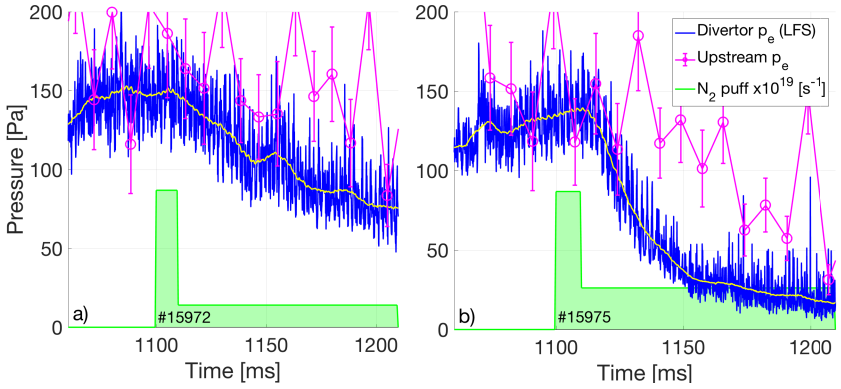

Figure 15. Evolution of upstream (magenta) and downstream (blue) pressure in discharges with high $\Gamma_{N_2} = 1.4 \times 10^{20} s^{-1}$ (A) and low $\Gamma_{N_2} = 3.2 \times 10^{20} s^{-1}$ (B) amount of seeding.

pressure was monitored by HRTS[6] at the position of separatrix calculated by magnetic reconstruction. Both upstream and downstream pressures were calculated using eq. 3.

It was observed that there is a significant drop of the downstream pressure following the injection of nitrogen and that the speed of the response and the magnitude of pressure drop can be controlled by the amount of injected nitrogen, as shown in Fig. 15. As expected, the effect of nitrogen was not restricted to the divertor only but also affected the upstream pressure. When this pressure drop (visible e.g. in Fig. 15B) was taken into account, it became difficult to determine whether the effect of nitrogen in the SOL is more significant than in the confined region.

In order to resolve this issue, a new series of experiments was performed, where the effect of nitrogen radiation inside the separatrix was compensated by the application of NBI heating. The effect of auxiliary heating on the upstream profiles was generally not too pronounced, so maximum available power of 450 kW was delivered into the plasma. Note that in a non-seeded discharge this would lead to access to H-mode but the presence of nitrogen clearly prevents it. Fig. 16 shows a comparison of two discharges with identical amount of nitrogen

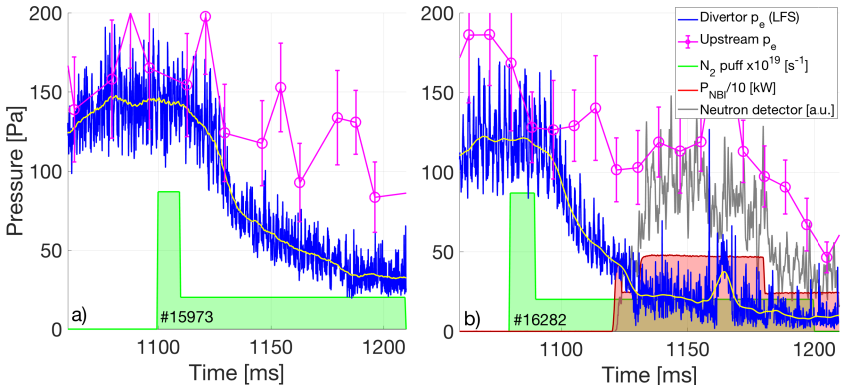

Figure 16. Evolution of upstream (magenta) and downstream (blue) pressure in ohmic (A) and NBI-heated (B) discharge with identical amount of seeding.

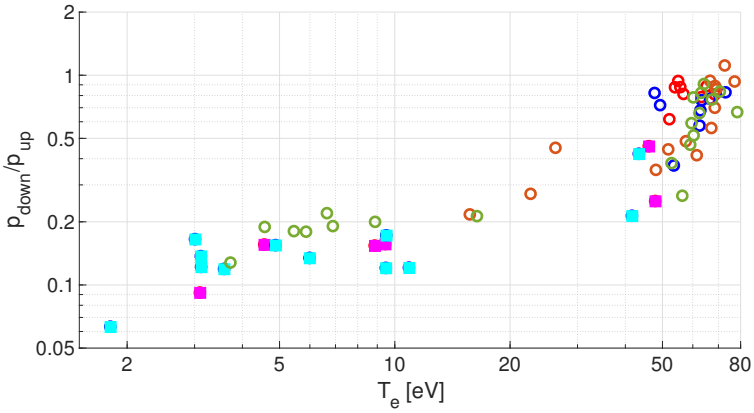

Figure 17. Ratio of downstream (p_{down}) and upstream (p_{up}) pressures as a function of maximum T_e at the outer target in different discharges with LFS nitrogen seeding. Square symbols indicate application of NBI.

seeding, where Fig. 16A was purely Ohmic and 16B was NBI-assisted. The upstream pressure partially recovers once the NBI heating reaches its peak value (at t=1135 ms) but the effect is not too pronounced as the pressure decreases again for t $>$ 1170 ms. This corresponds to a drop of signal from the neutron detector (gray line in Fig. 16B), which indicates that the absorption of the fast neutrals from the NBI systems is changing during the discharge. This behavior may be linked to a occurrence of large sawteeth at these times but the exact underlying mechanism is not well understood. The downstream pressure is not significantly affected by the application of NBI.

The achieved pressure drop is summarised in Fig. 17, where the ratio of the downstream and upstream pressures in all discharges with LFS nitrogen seeding is plotted against the target temperature. The lowest pressure fractions were achieved during the NBI phases (marked by squares in the figure) and represent a clear demonstration of partial detachment. Note that the shape of the dependency on T_e is quite different than observed at C-mod[20] and AUG [21]. This can be a consequence of the radiation of nitrogen in the confined plasma, which was not

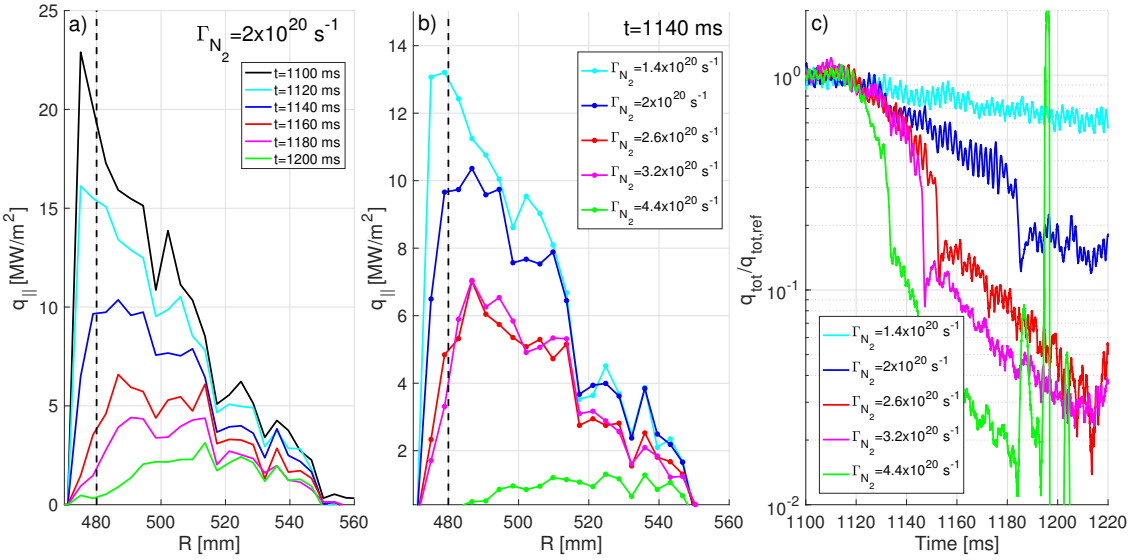

Figure 18. Temporal evolution of heat flux during a seeding experiment in the vicinity of the outer strike point (a), Heat flux profiles at t=1140 ms for varying amount of seeding (b) and ratio of integral heat flux at the outer target q_{tot} normalized to pre-seeding level $q_{tot,ref}$ (c). Solid lines show the combined LP+BPP array, dashed lines swept LPs.

so pronounced in larger devices.

4. Buffered heat flux at the outer target

The principal objective of operation in detached regime is to mitigate heat fluxes impinging onto the divertor targets, in order to avoid damage of the plasma-facing components. This is needed already in some of the contemporary machines (such as AUG) in high-power scenarios and it will be unavoidable for ITER and next-step machines. In order to evaluate the effect of impurity seeding on the heat fluxes, radial profiles of heat flux were constructed based on probe measurements at the outer target using eq. 4. Due to better spatial and temporal resolution, only results from combined LP+BPP array are used in the analysis.

Figure 18 summarises the heat flux measurements, with data from discharges, where nitrogen was introduced at the LFS. The impurity injection is causing large decrease of the heat flux close to the strike point (marked by vertical dashed line), reducing it more than factor of 10, while further away the reduction is less significant.

Instead of attempting to characterise the heat flux footprints during the nitrogen seeding, one can use the attached heat flux profile as a reference q_{ref} (black line in Fig.18A) and introduce a buffered heat flux q_B, the heat flux which has been removed from the footprint due to the presence of injected impurity:

$$q_B(t,R) = (q_{ref}(R) - q(t,R))/q_{ref}(R). \tag{5}$$

Since the effect of the nitrogen seeding is believed to be localised in the divertor region, we prefer not to map the profiles to the outer midplane but instead use the radial coordinate R

at the target. An example of the profiles of buffered flux q_B in case of moderate seeding at the LFS are shown in Fig. 19A. The profiles can be well characterised by an exponential decay

$$q_B(R) = A_B exp(-(R - R_{OSP})/\lambda_B) \tag{6}$$

Due to the limited data set it is difficult to determine if exponential profile is the best fit of the decay, neither it is backed by any hypothesis on underlying physical processes. However, it allows to characterise the main features of the buffering: the magnitude of buffering at the strike point A_B and the spatial extend of the buffering λ_B. Note that the values of λ_B are significantly larger than the λ_q in the attached plasmas (typically between 20-40 mm at outer target).

These parameters are expected to be primarily dependent on the inventory of nitrogen in the plasma. Indeed, both parameters exhibit approximately linear dependencies on the N_2 content, as shown in Fig. 20. Only fits with error lower than 50% were used for this analysis, which discarded in particular a number of fits at low nitrogen content. In such cases the buffering of heat fluxes is small and so the q_B is subject to higher level of fluctuations. Note that in order to calculate the N_2 inventory, one must consider the removal of nitrogen from the plasma either by pumping of neutrals or by chemical reactions which increase the nitrogen wall inventory [24]. An upper estimate of this flux can be deduced from the LFS seeding scan, where the lowest seeded amount $\Gamma_{N_2} = 1.4 \times 10^{20} s^{-1}$ results only in slowly varying effects on the target profiles, which is an indication of being close to equilibrium in terms of nitrogen injection and removal. We assume that all the discharges in the scan follow a common trajectory and choose the right amount of nitrogen removal to align the dependencies of fitted parameters on nitrogen content in Figs. 7B, 20A and 23. This value was found to be $\Gamma_{N_2,out} = 1.0 \times 10^{20} s^{-1}$, which is close to the upper estimate described earlier. In future this rough estimation should be supported by dedicated experiments, focused e.g. on plasma recovery after series of short seeding pulses. In case of the A_B parameter, the dependence is coherent across the whole LFS seeding scan, in case of λ_B there appears to be a reduced applicability of the exponential fit at low amount of seeded impurity. In this case the heat flux profile is not significantly perturbed and fluctuations in the heat flux may interfere with the fitting.

5. Characterisation of the partially detached divertor footprints

The divertor heat fluxes in attached conditions are typically mapped to outer midplane and characterised by a function proposed by Eich in Ref. [22], which is a convolution of an exponential decay (with power decay length λ_q) and the Gaussian broadening of the profile (with characteristic width S) given by

$$q_s = \frac{q_0}{2} exp\left((\frac{S}{2\lambda_q})^2 - \frac{s}{\lambda_q f_x} \right) \cdot erfc(\frac{S}{2\lambda_q} - \frac{s}{S f_x}) + q_{BG}, \tag{7}$$

where f_x is the flux expansion at the target, q_0 the peak heat flux, q_{BG} the background heat flux due to radiation and s is the spatial coordinate running along the target in poloidal

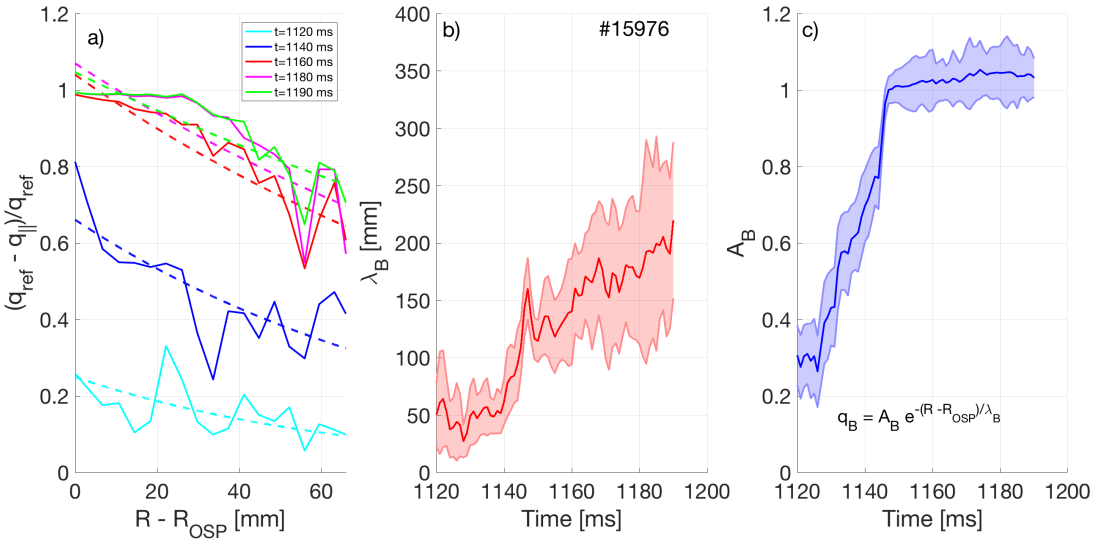

Figure 19. Buffered heat flux during discharge #15976 (A) and the time evolution of the fitting parameters λ_B (B) and A_B (C).

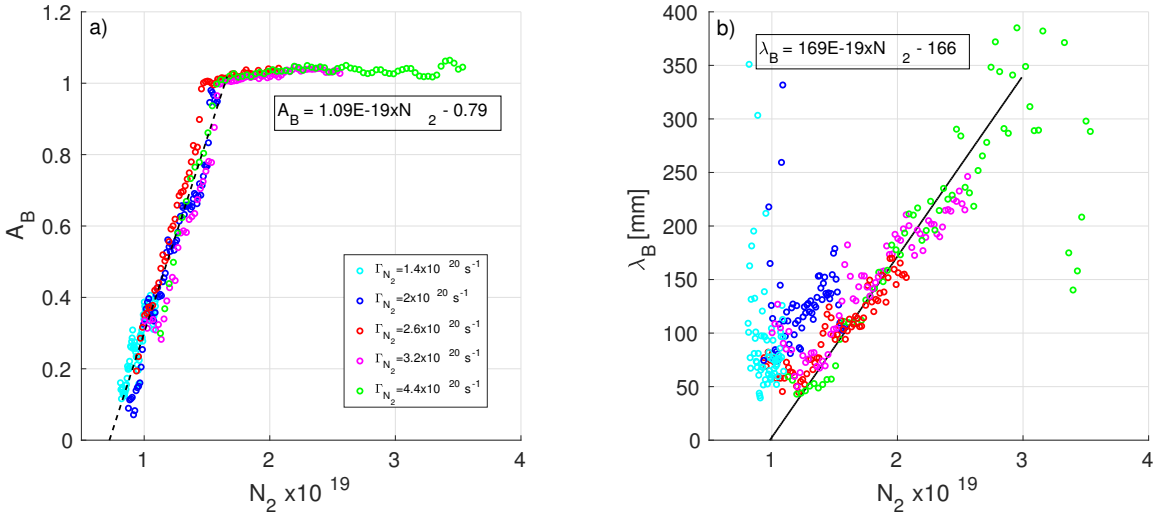

Figure 20. Dependence of buffer fit parameters A_B (left) and λ_B (right) on the content of nitrogen in the discharge. Linear fits showed by black lines.

direction. This function reflects the assumption that the divertor target profile is partially determined by upstream conditions (exponential decay) and partially by processes in the divertor region (collisions and finite Larmor effects [12]). The decaying part of the profile can be then approximated by an exponential decay with characteristic length λ_{int}[23]

$$\lambda_{int} = \lambda_q + 1.64S \tag{8}$$

This characterisation proved to be successful in accurate description of heat flux profiles on a number of machines [22]. However, its domain of applicability is limited by the physical picture described above, which does not include e.g. dissipative processes, where part of the

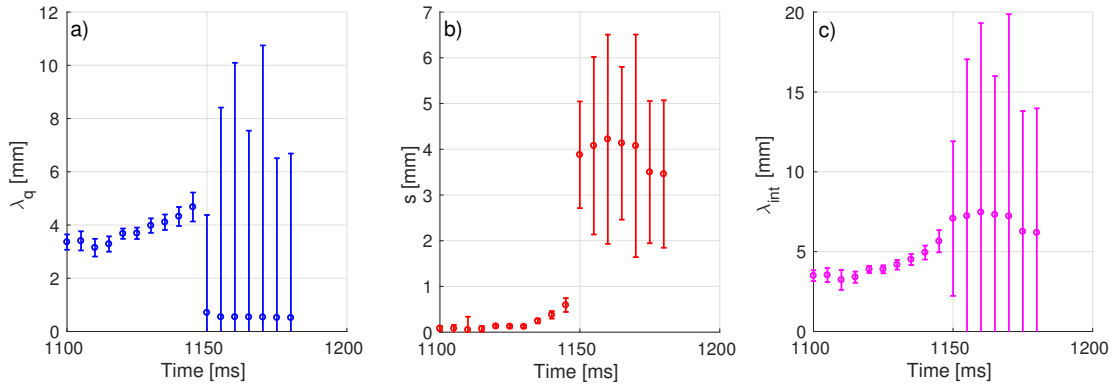

Figure 21. Time evolution of λ_q (A), s (B) and λ_{int} (C) in shot #15976

power is converted into radiation. With 5 degrees of freedom available, the formula 7 can be still technically applied to fit the target profiles even when such processes are significant (as it is the case in detached plasmas) but in such case the fitting parameters λ_q and S are losing their original meaning. In order to illustrate it, we have analyzed discharge #15976 (Γ_{N_2} = 4.4 $\times 10^{20}$ s^{-1}) and plotted the time evolution of λ_q, S and λ_{int} in Fig. 21. It can be seen that the fitted λ_q is increasing during the initial part of the seeding until the transition to detachment (around t=1150 ms), when it sharply drops and the quality of the fit significantly decreases. However, the main parameters, which determine it according to L-mode multi-machine scaling by Eich[35] (B_T and q_{cyl}), remain constant during the flat-top. The apparent change of λ_q is a consequence of different physical processes influencing the divertor footprint - the effect of nitrogen seeding has different nature than a Gaussian broadening of the profile.

In order to analyse the profiles in detached plasmas (as shown in Fig. 18A,B), a new set of parameters should be implemented to allow multi-machine comparisons. The approach presented in the previous section is feared to be limited to particular conditions of the COMPASS divertor and may not be applicable on other tokamaks. Since the problem of heat fluxes is mostly an engineering issue, we propose to charaterise the heat fluxes by a set of parameters, which are suitable for evaluation of safety issues related to PFCs. These are the following: (i) *peak heat flux* q_{peak} being the maximum of heat flux (from which the background radiation q_{BG} is substracted), (ii) *divertor power fraction* $f_{div} = 2\pi R \int q_{||}(s) sin(\alpha(s)) ds / P_{sep}$ being the fraction of power crossing the separatrix which reaches the target and (iii) *footprint spreading factor* S_f - minimal distance along the target over which $1 - 1/e \sim 63\%$ of the power is deposited, normalized by the expected footprint width in an idealized case of attached plasmas in absence of spreading (S=0) $\lambda_q f_x$.

In case of attached plasmas with constant angle of incidence α, one can relate the new set of parameters with those implemented by Eich:

$$q_{peak} = q_0 \frac{\lambda_q}{\lambda_{int}}; f_{div} = 2\pi R f_x q_0 \lambda_q sin(\alpha)/P_{sep}; S_f = \lambda_{int}/\lambda_q = 1 + 1.64 S/\lambda_q \quad (9)$$

Time traces shown in Fig. 22 show evolution of the new set of parameters obtained at the outer target. It can be seen that while f_{div} and q_{peak} are changing dramatically during the

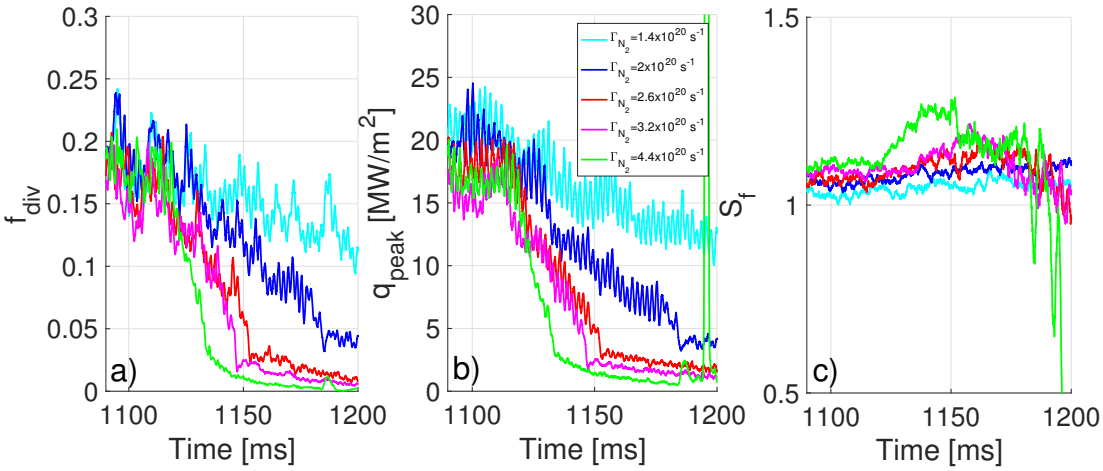

Figure 22. Time evolution of f_{div} (A), q_{peak} (B) and S_f (C) in discharges with LFS nitrogen seeding

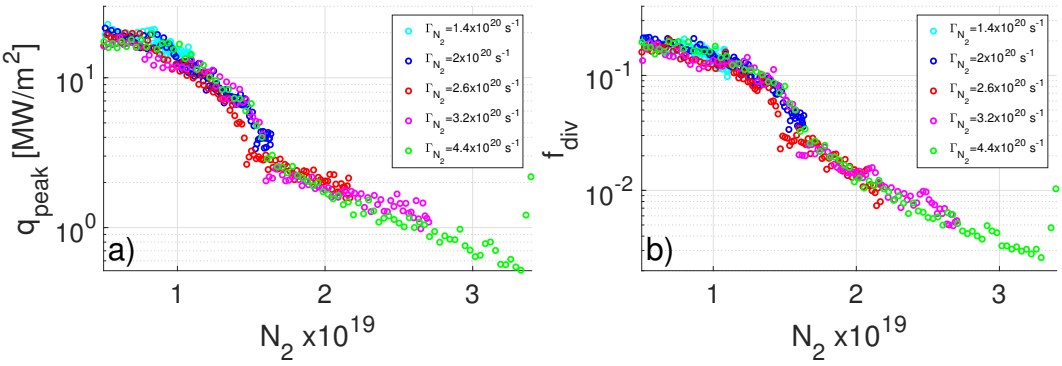

Figure 23. Dependence of parameters q_{peak} and f_{div} on the content of nitrogen in the discharge

impurity seeding, the third parameter S_f appears to be rather invariant.

As with the parameters describing the buffered heat flux, one can again expect that the main factor influencing their evolution is the nitrogen content in the plasma. The dependencies (shown in Fig. 23) are, however, more complex than in case of q_B. Both q_{peak} and f_{div} are sharp decreasing of at low nitrogen content. This trend is interrupted, when the inventory exceeds 1.5×10^{19} particles and transits into a slower exponential decay.

6. Comparison with the detachment scaling model

A recent model for detachment scaling introduced by Goldston [26] allows to predict the nitrogen concentration required for detachment. In order to compare COMPASS data with the results presented in [26], it is necessary to account for the fact that our experiments were performed in L-mode, where the power decay length is expected to be larger than in H-mode. Indeed, the heuristic drift model [28] predicts $\lambda_{q,HD}$ = 2.5 mm, while analysis of the footprint at outer target prior to seeding show λ_q = 4 mm. In order to rescale the results obtained for

AUG in [26], we need to calculate the factor $P_{sep}/((\lambda_q/\lambda_{q,HD})^{8/7} < B_p > (n_{sep}/n_{gw})^2 l_{||}^*)$, which has a value of 200 (P_{sep} = 230 kW, $< B_p >$ = 0.16 T, n_{sep} = 1.7x10^{19} m^{-3}, n_{gw} = 21.8x10^{19} m^{-3}, L_{con} = 3.9 m, q_{cyl} = 4.2, $l_{||}^*$ = 0.54). Using data from Table 2 in [26], one finds the predicted impurity fraction c_z = 7.6%, which is higher than on JET or AUG but lower than the fraction predicted for ITER.

Unfortunately, the analysis of experimental data does not allow precise confrontation of this prediction. The estimation based on spectral measurements presented in section 3.2 allows only for rough comparison, since the key parameters τ and ΔL are not known with sufficient precision. Another rough estimate of nitrogen concentration can be obtained from the knowledge of nitrogen content, where we see an abrupt decrease of power delivered to the divertor at 1.5$\times$ 10^{19} particles. Given the approximate vessel volume of 1 m^3 and the line-averaged density of 4.0$\times$ 10^{19} m^{-3}, the c_z would be 37% if nitrogen would be distributed uniformly, which seems too high for the plasma to sustain operation. The most realistic estimate can be obtained from calculations of the cooling power $P_{cool} = c_z n_e^2 L_z$, which as seen in Fig. 18 can compensate almost the whole P_{sep}. The radiative loss function L_z can be approximately determined from Fig. 3 in [29] as 2$\times$10^{-32} Wm^3, which yields c_z of 5 percent, which is consistent with Goldston's prediction.

7. Conclusions

Nitrogen seeding was proved to be an efficient tool for reduction of divertor pressure and heat flux in a series of dedicated L-mode discharges at COMPASS. The plasma response to the seeding is in general dependent on the location of the seeding, with more favourable results being achieved with seeding in the vicinity of the outer strike point. The nitrogen radiation is not restricted to the divertor region but affects also the confined plasma, which results in considerable upstream temperature drop. This effect can be compensated by the application of additional heating, without a significant effect on the downstream pressure. During the NBI-assisted discharges the ratio of upstream and downstream pressure changed by a factor of 10, which is a clear demonstration of partial detachment.

In order to characterise the effect of nitrogen seeding on the divertor footprint, the buffered heat flux q_B was introduced. Buffered heat flux at COMPASS can be well approximated by an exponential decay with large characteristic length. Both parameters describing q_B exhibit a linear dependence on the nitrogen content, however this feature remains to be tested on data from other machines. Also, a more generic way of characterising the heat fluxes was proposed, to answer the practical questions related to the engineering limits of the plasma-facing components. The peak heat flux q_{peak} and divertor power fraction f_{div} again depend strongly on the nitrogen content, however the footprint spreading factor S_f is surprisingly insensitive and remains constant during the seeding.

Acknowledgments

First author would like to thank R. J. Goldston for valuable discussion related to his

detachment scaling model and T. Eich for discussion on the λ_q scaling. This work has been carried out within the framework of the EUROfuison Consortium and has received funding from the Euratom research and training programme 2014-2018 and 2019-2020 under grant agreement No 633053. The views and opinions expressed herein do not necessarily reflect those of the European Commission. It was supported by projects Czech Science Foundation GA15-10723S, GA16-14228S, MYES Project #LM2011021 and IAEA CRP F13019 - Research Contract No. 22727/R0. The views and opinions expressed herein do not necessarily reflect those of the European Commission. Simulations for this work were performed at National Computational center IT4Innovations and International Fusion Energy Research Centre cluster HELIOS.

[1] M. Komm et al., proceedings of the 44^{th} EPS confererence (2017) **P1.118**
[2] Tsv. K. Popov et al., Plasma Phys. Control. Fusion **51** (2009) 065014
[3] J. Adamek et al. Nucl. Fusion **57** (2017) 116017
[4] J. Mlynar et al., Rev. Sci. Instr. **83** 10E531 (2012)
[5] A. Havranek et al., Fusion Eng. and Design **123** (2017) 857-860
[6] M. Aftanas et al., Rev. Sci. Instr. **83** (2012) 10E350
[7] T. Eich et al. Nucl. Fusion **58** (2018) 034001
[8] P. C Stangeby *The plasma boundary of magnetic fusion devices* IOP Publishing (2000)
[9] Yu. Igitkhanov and G. Janeschitz J. Nucl. Mater. **99** (2001) 290-293
[10] S.Y. Allan et al. Plasma Phys. Control. Fusion **58** (2016) 045014
[11] T. Eich et al. Phys. Rev. Lett. **107** 2011 215001
[12] B. Sieglin et al. Plasma Phys. Control. Fusion **58** (2016) 055015
[13] J. P. Gunn et al. Nucl. Fusion **57** (2017) 046025
[14] A.S. Kukushkin et al. Nucl. Fusion **49** (2009) 075008
[15] T.W. Petrie et al. J. Nucl. Mat. **241-243** (1997) 639-644
[16] A. Podolnik et al. Plasma Phys. Control. Fusion **60** (2018) 085008
[17] K. Jirakova et al. Proceedings of the 45th EPS conference, Prague (2018) P5.1081
[18] J. Adamek et al. Nucl. Fusion **57** (2017) 022010
[19] A.G. McLean et al. J. Nucl. Mat. **463** (2015) 533-536
[20] B. Lipschultz et al., Fusion Sci. Tech. **51** (2017) 369-389
[21] I.P. Perez et al. Nucl. Mat. Energy **12** (2017) 182-186
[22] T. Eich et al., Nucl. Fusion **53** (2013) 093031
[23] M.A. Makowski Phys. Plasmas **19** (2012) 056122
[24] F.L. Tabares J. Nucl. Mater. **337-339** (2005) 867-871
[25] D. Naydenkova et al. Appl. Optics **53** (2014) 8123-8130
[26] R. J. Goldston et al. Plasma Phys. Control. Fusion **59** (2017) 055015
[27] J. Horacek et al. 45th EPS Conference, Prague (2018) P5.1030
[28] R. J. Goldston et al. Nucl. Fusion **52** (2012) 013009
[29] A. Kallenbach et al. Plasma Phys. Control. Fusion **58** (2016) 045013
[30] A. Scarabosio et al. J. Nucl. Mater. **438** (2013) S426S430
[31] F. Reimold et al. J. Nucl. Fusion **55** (2015) 033004
[32] A. Loarte Plasma Phys. Control. Fusion **43** (2001) R183-R224
[33] A. Kallenbach et al., Nucl. Fusion **57** (2017) 102015
[34] S. S. Henderson et al., Nucl. Fusion **58** (2018) 016047
[35] T. Eich et al., J. Nucl. Mat.**438** (2013) S72-S7
[36] J. Seidl et al., Nucl. Fusion **57** (2017) 126048
[37] A. V. Melnikov et al., Plasma Phys. Control Fusion **57** (2015) 065006
[38] T. Markovic et al., Proceedings of the 44th EPS conference (2017) P5.140
[39] F. Reimold et al. Nucl. Fusion **55** (2015) 033004

[40] S. Potzel et al. Nucl. Fusion **54** (2014) 013001
[41] S. Potzel et al. J. Nucl. Mat. **438** (2013) S285-S290
[42] S. Potzel et al. J. Nucl. Mat. **438** (2013) S285-S290
[43] A. Stepanenko et al. Phys. of Plasmas **25** (2018) 012305
[44] S. I. Krasheninnikov et al. Nucl. Mat. Energy **12** (2017) 1061-1066
[45] S. I. Krasheninnikov et al. Phys. Plasmas **23** (2016) 092505